Detailed analysis of the synthesis and structure of MAX phase $(Mo_{0.75}V_{0.25})_5AlC_4$ and its MXene sibling $(Mo_{0.75}V_{0.25})_5C_4$

Rose M. Snyder[a], Mikkel Juelsholt[c], Curran Kalha[d], Jason Holm,[e] Elisabeth Mansfield,[e] Tien-Lin Lee[f], Pardeep K. Thakur[f], Aysha A. Riaz[d], Benjamin Moss[g], Anna Regoutz[d], Christina S. Birkel[a,b*]

[a]School of Molecular Science, Arizona State University, Tempe, AZ 85281, USA
[b]Department of Chemistry and Biochemistry, Technische Universitaet Darmstadt, 64287 Darmstadt, Germany
[c]Department of Materials, University of Oxford, Oxford, OX1 3PH, UK.
[d]Department of Chemistry, University College London, London, WC1H 0AJ, UK.
[e]Applied Chemicals and Materials Division, National Institute of Standards and Technology, Boulder, CO 80305, USA
[f]Diamond Light Source, Harwell Science and Innovation Campus, Didcot, OX11 0DE, UK.
[g]Department of Chemistry, Molecular Science Research Hub, White City Campus, Imperial College London, London W12 0BZ, UK.
*Corresponding Author: Christina Birkel – School of Molecular Science, Arizona State University, Tempe, AZ 85281, USA and Department of Chemistry and Biochemistry, Technische Universitaet Darmstadt, 64287 Darmstadt, Germany; Email: christina.birkel@asu.edu

Abstract: MAX phases with the general formula $M_{n+1}AX_n$ are layered carbides, nitrides and carbonitrides with varying stacking sequence of layers of M_6X octahedra and the *A* element depending on *n*. While "211" MAX phases (*n* = 1) are very common, MAX phases with higher *n*, especially *n* ≥ 3, have hardly been prepared. This work addresses open questions regarding the synthesis conditions, structure, and chemical composition of the "514" MAX phase. In contrast to literature reports, no oxide is needed to form the MAX phase, yet multiple heating steps at 1,600 °C are required. Using high-resolution X-ray diffraction, the structure of $(Mo_{1-x}V_x)_5AlC_4$ is thoroughly investigated and Rietveld refinement suggests *P*-6*c*2 as the most fitting space group. SEM/EDS and XPS show that the chemical composition of the MAX phase is $(Mo_{0.75}V_{0.25})_5AlC_4$. It was also exfoliated into its MXene sibling $(Mo_{0.75}V_{0.25})_5C_4$ using two different techniques (using HF and an HF/HCl mixture), which leads to different surface terminations as shown by XPS/HAXPES measurements. Initial investigations of the electrocatalytic properties of both MXene versions show that depending on the etchant, $(Mo_{0.75}V_{0.25})_5C_4$ can reduce hydrogen at 10 mA cm^{-2} with an overpotential of 166 mV (HF only) or 425 mV (HF/HCl) after cycling the samples, which makes them a potential candidate as an HER catalyst.

Keywords: *MAX phase, MXene, $(Mo_{0.75}V_{0.25})_5AlC_4$, $(Mo_{0.75}V_{0.25})_5C_4$, synchrotron XRD, STEM-in-SEM, electrocatalysis*

As technology advances, we aim to discover practical materials that can meet the needs of our growing society, providing certain functionalities (e.g. energy conversion, magnetism) and enhanced processibility and stability. A class of materials, MAX phases, have the potential to meet most of these needs because of their distinct crystal and electronic structure combined with their versatile chemical composition. They have properties that are considered both ceramic and metallic, making them resistant to oxidation and thermal shock, thermally and electrically conductive, and highly machinable.[1–3] Consequentially, they have become attractive materials for applications, such as coatings,[4] catalysts[5] and electrical contacts.[6]

MAX phases are ternary layered carbides, nitrides and carbonitrides with the general formula $M_{n+1}AX_n$, where *M* is an early transition metal, *A* is

typically a group 13 or 14 metal, *X* is carbon and/or nitrogen, and *n* is an integer, usually 1, 2, or 3. Their structure consists of layers of edge-sharing M_6X octahedra (grey polyhedra in Figure 1) interleaved with layers of the *A* element (light blue in Figure 1).[1,2] Depending on *n*, the stacking sequence changes (compare a-c in Figure 1). To simplify the naming convention, MAX phases are occasionally referred to as 211 (*n* = 1), 312 (*n* = 2), 413 (*n* = 3) phases and so on, depending on the *n* value. Because the composition is variable, there are almost unlimited opportunities to synthesize additional members in this family. After their initial discovery in the 1960s[7], and a large drive in research around the turn of the century[8–10], more than 155 members of this material class have been synthesized, including solid solution and ordered MAX phases.[2] Almost all the known MAX phases are 2 (*n* = 1), 3 (*n* = 2), and 4 (*n* = 3) atomic metal-layered

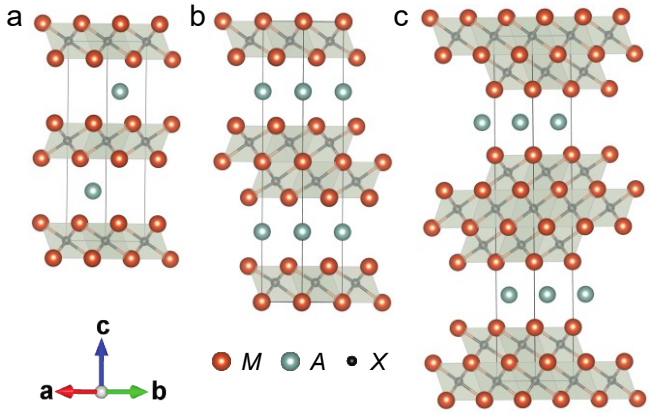

***Figure 1**: Representations of "211", "312" and "413" MAX phases M_2AX (a), M_3AX_2 (b), and M_4AX_3 (c), respectively. The M element is represented by orange atoms, the A element is light blue, and X is black. This demonstrates the different stacking sequences of layers of M_6X octahedra (grey polyhedra) and A layers as well as the increasing c lattice parameters along c with increasing n.*

structures,[2] which means the discovery of higher MAX phases ($n \geq 4$) is the next crucial step to expanding this family of materials. It has been shown that mechanical properties and stability are affected by a change in *n* and consequentially are linked to the crystal structure, i.e. stacking sequence of the M_6X and *A* layers.[11,12] Additionally, MXenes synthesized from MAX phases with higher *n* are more likely to be thermodynamically stable[13] and less susceptible to oxidation,[14] which is a key advantage if MXenes are used for specific applications. Besides, the possibility of enhanced properties, such as better EMI (Electromagnetic Interference) shielding capabilities and higher electrical conductivity, has also been mentioned.[18]

Several higher MAX phases, including Ta_6AlC_5[15] and $(Ti_{0.5}Nb_{0.5})_5AlC_4$,[16] have been previously synthesized, though they were found to be a side product of another MAX phase and not available as a pure phase product. Additionally, Ti_5SiC_4 is a predicted metastable species that has not yet been synthesized.[17] In 2019, Deysher *et al.* updated the MAX phase family with Mo_4VAlC_4, with 5 metal layers, and no other MAX phase side phases.[18] This 514 MAX phase was also etched and delaminated to form the two-dimensional (2D) MXene analogue, Mo_4VC_4. MXenes share the same structure as their MAX phase counterparts but have been etched to remove the *A* layer, leaving behind lamellae of only M_6X edge-sharing octahedra.[19–21]

MXenes have the formula $M_{n+1}X_nT_x$, where *M*, *X*, and *n* correspond with the elements present in the parent MAX phase, and T_x represents the terminating groups on the surface evolving during the exfoliation process.[20] For simplicity, T_x is commonly omitted from the formula name. The *A* layer is typically removed with hydrofluoric acid (HF), a weak acid that selectively reacts with aluminum.[22] However, HF is severely toxic (fatal!) to humans who are exposed to it,[23] which means that reducing or eliminating the HF concentration is desirable when possible. Similar to MAX phases, MXenes are very interesting materials, owing to their electronic structure and mechanical properties, offering a multitude of potential applications, from battery materials[24] to catalysts[25,26] and sensors.[27]

There are two interesting observations that Deysher *et al.* reported in their study, one concerning the MAX phase synthesis and one concerning its crystal structure. (i) The authors report that the Mo_4VAlC_4 synthesis requires the addition of 0.05 mol of V_2O_3 to the precursor mixture to form the MAX phase, and its exclusion leads to a product that only consists of Mo_2C and VC.[18] The authors hypothesized that the oxygen in the mixture acted as a catalyst that also produced heat through thermal reduction to push the reaction forward.[18] (ii) While MAX phases typically crystallize in a hexagonal structure with space group $P6_3/mmc$, they proposed this MAX phase to crystallize in space group *P*-6*m*2 due to a herringbone-style

ordering found in the M_6X octahedral layer.[18] However, this was still unconfirmed, and the structure of the $(Mo_{1-x}V_x)_5AlC_4$ MAX phase has yet to be determined. Additionally, the exact stoichiometry of the solid solution MAX phase (and respective MXene) also remains open. Deysher *et al.* report successful synthesis only for a 4:1 ratio between Mo and V, while 3:2, 2:3 and 1:4 ratios do not lead to the MAX phase.[18]

Addressing the curious synthesis conditions and open structural questions raised by Deysher *et al*., we revisit the preparation of $(Mo_{1-x}V_x)_5AlC_4$ and add a thorough structural investigation by means of high-energy synchrotron X-ray diffraction and Pair Distribution Analysis (PDF). We also utilize 4-dimensional scanning transmission electron microscopy in a scanning electron microscope (STEM-in-SEM) with selected area electron diffraction (SAED),[28,29] to confirm our findings. Insights into the elemental composition were provided by soft and hard X-ray photoelectron spectroscopy (SXPS/HAXPES) and electron dispersive spectroscopy (EDS), both of which confirm the Mo to V ratio (3:1). Additionally, we synthesize the MXene, $(Mo_{0.75}V_{0.25})_5C_4$, and investigate the effect of etching with HF/HCl (instead of only HF) on the electrocatalytic properties for the hydrogen evolution reaction (HER), a process that produces clean fuel for future technologies.

Results and Discussion

MAX phase: $(Mo_{0.75}V_{0.25})_5AlC_4$

Using data collected at the 11-BM high-resolution X-ray diffractometer (HR-XRD) at Argonne National Laboratory, the reflections of the MAX phase samples were indexed using the GSAS-II crystallography analysis software. Indexed data were used to design unit cell models of $(M_{0.75}V_{0.25})_5AlC_4$ with the appropriate space group (*Supporting Information Fig. SI-1*). Traditional MAX phases have a hexagonal $P6_3/mmc$ space group, while this particular "514" phase does not. The powder XRD reflections do not agree with a $P6_3/mmc$ space group and past work has shown that Mo_4VAlC_4[18] has a herringbone structure (Figure 2b) in the M_6X layer which is not a common crystal stacking order for these materials.[2] However, while the space group is not the same as other MAX phases, we still observe evenly spaced (00*l*) peaks in the HR-XRD (Figure 3a) and STEM data (Figure 4) show a hexagonal, layered structure, implying that our product is closely related in structure to $n \leq 3$ MAX phases.

Figure 3a shows the high-resolution XRD data (orange dots), their Rietveld refinement (dark grey line) and model/literature data used for the structural analysis (GSAS-II). The product consists of $(Mo_{0.75}V_{0.25})_5AlC_4$ as the main phase (blue markers in Figure 3a) with $(Mo,V)_4AlC_3$ (a=2.9269(1) Å, c=22.753(1) Å) as a minor side phase (red markers in Figure 3a). Please note that the side phase is likely a solid solution between Mo and V, however the exact chemical composition cannot be determined based on the very low intensity of the peaks. However, for the main product, we can confirm the composition of $(Mo_{0.75}V_{0.25})_5AlC_4$ based on synthesis parameters set, as well as EDS and XPS measurements (Figures 5 and 11, respectively). Aside from these two MAX phases, we note that there are several peaks that belong to a phase (*Supporting Information Fig. SI-2*) that we have not been able to identify, despite comparing the peaks to all known carbides, oxides and intermetallics that would be feasible.

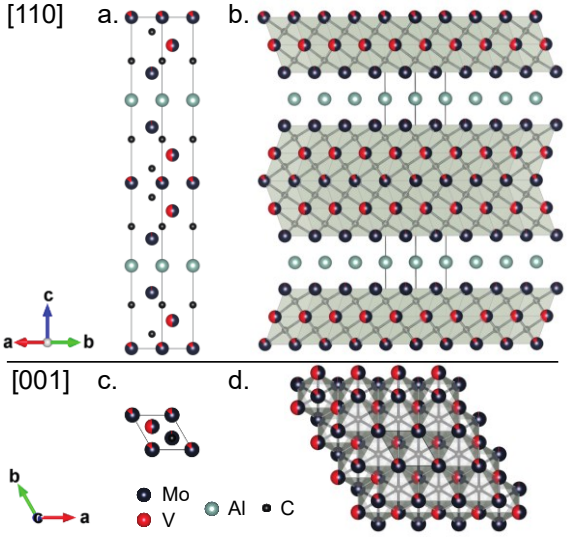

Figure 2: *The [110] projection of the unit cell of $(Mo_{0.75}V_{0.25})_5AlC_4$ (a), as well as the expanded structure of the [110] projection (b). The [001] unit cell projection (c) is also shown and expanded (d). Mo (navy) and V (red) are filled according to relative occupancies determined by Rietveld refinement. Black atoms represent carbon and light blue atoms represent aluminum. The herringbone structure can be seen in (b).*

For the "514" MAX phase, two space groups were found to be possible matches for the reflections as they were indexed, $P\bar{6}m2$ and $P\bar{6}c2$.[30] (*Supporting Information Fig. SI-3a, 3b)* Rietveld refinement of the

high-resolution data showed a better fit for the *P*-6*c*2 crystal structure (blue peak positions in Figure 3a). In accordance, real space Rietveld refinement of the obtained Pair Distribution Function (PDF) also confirms that the synthesized "514" phase can be best described using a structure with the space group *P*-6*c*2 (Figure 3), where *P*-6*m*2 leads to a worse fit (R_w = 0.346 for *P*-6*m*2 (*Supporting Information Fig. SI-4a) vs* R_w *= 0.146 for P*-6*c*2 (Figure 3b)). However, as shown in Figures SI-3 and *SI-4a*, a structure with space group $P6_3/mmc$ cannot fit the data, which further supports that the "514" phase does not crystallize in the same space group as most other MAX phases. Please note, that as it stands, $P6_3/mmc$ can very likely be ruled out and further analysis of the present diffraction data suggests that the 514 phase crystallizes in space group *P*-6*c*2. However, the space group *P*-6*m*2 should not be disregarded fully due to the presence of multiple side phases in the MAX phase product and with that uncertainties as far as the refinements go.

Structurally, $(Mo_{0.75}V_{0.25})_5AlC_4$ has 9 total layers in the M_6X octahedral lamella (5 metal, 4 carbon), interleaved by a single Al layer and the unit cell consists of 2 formula units. The Mo/V-C bond lengths are 3.59964/2.01087 Å and the Mo/V-Al bond lengths are 2.85682/4.13221 Å. The *a*-lattice parameter and the *c*-lattice parameter of the "514" MAX phase are refined to 2.98558(5) Å and 27.9813(3) Å, respectively. These lattice parameters are close to those reported by Deysher *et al.* (a=~3.00 Å, c=28.22 Å).[18] Refinement of the occupancies of the $(Mo_{1-x}V_x)_5AlC_4$ shows that the sample is a solid solution with x = 0.24, where Mo and V occupy *M* sites randomly. This matches results from elemental analyses very well (Figure 5, Table I). However, the data also imply that there is a much stronger Mo presence on the outermost and central layers, at the 4i and 2a Wyckoff positions, respectively.

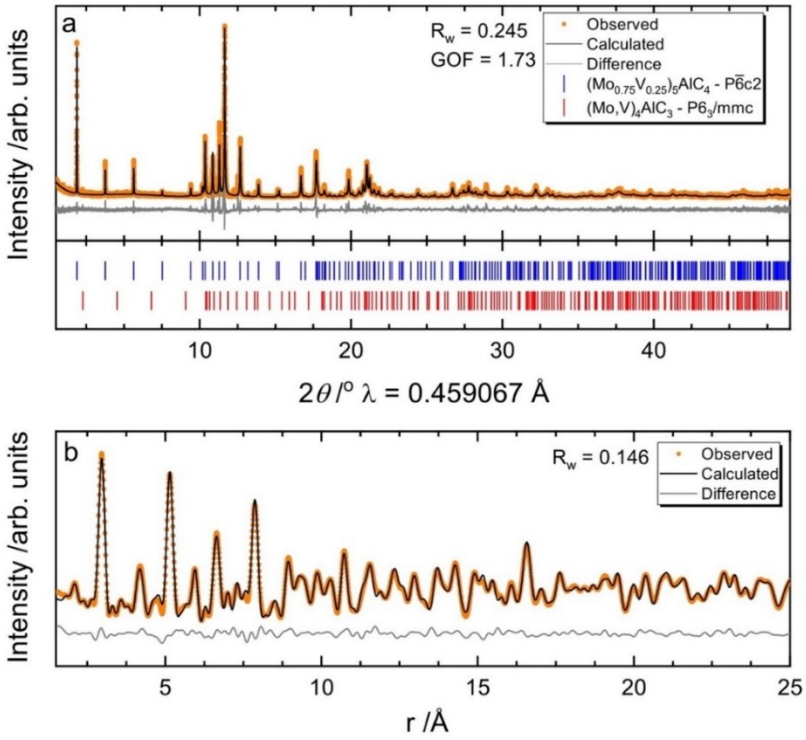

Figure 3: *(a) Rietveld refinement of high-resolution synchrotron XRD data collected from 11-BM at Argonne National Lab. Orange dots show observed diffraction pattern, the black line shows the calculated diffraction for a crystal structure with a P-6c2 space group, and the dark gray line shows the difference between the calculated and observed data. Markers are included below the refinement showing the (hkl) positions for the two known present phase; the main phase,* $(Mo_{0.75}V_{0.25})_5AlC_4$ *(blue) and the side phase,* $(Mo,V)_4AlC_3$ *(red). (b) Real-space Rietveld refinement of the Pair Distribution Function of the* $(Mo_{0.75}V_{0.25})_5AlC_4$ *sample. Black dots represent PDF, the black line is the calculated PDF for a sample with a P-6c2 space group, and the gray line is the difference between the calculated and observed PDFs.*

STEM micrographs of the multilayer MXene (Figure 4) show that the center Mo/V layer and certain areas along the surface are distinctly brighter than the rest of the sample (red arrows in Figure 4 c, d), which could confirm an elemental imbalance at those layers.

To investigate the formation mechanism, *ex-situ* laboratory XRD data were collected for samples heated at regular intervals from 300-1600 °C and then at each heating stage once the sample reached its holding temperature (*Supporting Information Fig. SI-5*). Samples were prepared from pure elemental powders of molybdenum, vanadium, aluminum and carbon and those elemental powders are the only species present in the sample from 300-600 °C. Intermetallics first begin to appear at 900 °C, with Mo_3Al forming first. At 1200 °C, carbides begin to form, including Mo_2C, Mo_3Al_2C, and $(Mo_{1-x}V_x)_2AlC$. The target MAX phase is not observable until 1600 °C, along with $(Mo_{1-x}V_x)_4AlC_3$, $(Mo_{1-x}V_x)_3AlC_2$ and the same intermetallics and carbides. Once $(Mo_{1-x}V_x)_5AlC_4$ forms, each additional run at 1600 °C for 6 h reveals a higher amount of $(Mo_{1-x}V_x)_5AlC_4$ and the quantities of the side phases begin to decrease until the sample has been processed 3 times at 1600 °C for 6 h (18 h total). The final product includes a small amount of the Mo/V-based "413" MAX phase, as well as a phase that we have not been able to identify. Intermittently (once the sample has been processed at 1600 °C for 6h – 12 h), we can see the presence of 3 different MAX phases, the "514", the "413", and interestingly, a "312" phase. Molybdenum- and vanadium- based 312 MAX phases do not form,[31] though they can exist as 312 alloys with metals like Ti or Cr.[32,33] This species was highlighted in the previous paper regarding the synthesis of Mo_4VAlC_4,[18] but to the best of our knowledge, this phase does not exist as a stable, phase pure product, though it is possible that it forms as a metastable intermediate species.

As far as the synthesis conditions are concerned, Deysher *et al.* noted that the addition of 0.05 mol V_2O_3 was required to produce the "514" MAX phase.[18] However, our synthesis did not require the addition of any oxides and does not show any oxide intermediate species (crystalline or amorphous) during the *ex-situ* measurements (*Supporting Information Figs. SI-4b-4e, SI-4*).

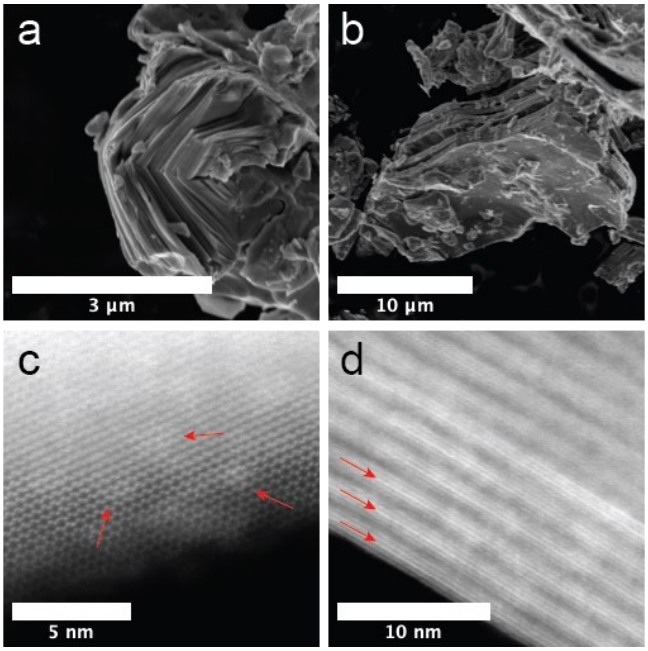

Figure 4: *SEM micrographs of $(Mo_{0.75}V_{0.25})_5AlC_4$ (a) and ML-$(Mo_{0.75}V_{0.25})_5C_4$ after etching in HF for 8 d (b). The separation of layers is apparent after acid treatment. Additionally, STEM micrographs of the surface (c) and edge sites (d) of the ML-MXene show the hexagonal, 5 metal-layered structure, Arrows have been added to highlight some areas where atoms appear brighter.*

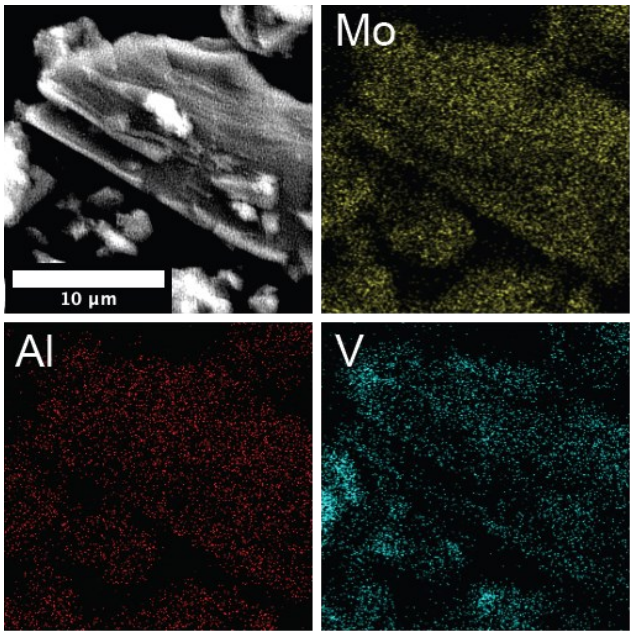

Figure 5*: EDS data collected for a selected area of the $(Mo_{0.75}V_{0.25})_5AlC_4$ MAX phase. Mo, Al, and V are represented by yellow, red, and light blue areas, respectively. Mo and V are evenly present across the sample, though bright spots in V may indicate the presence of VO/VC side products. Based on atomic weight percent, the Mo:V ratio is 2.7:1.0. The low Mo:V ratio is likely due to additional V-based species present in the sample.*

Table I: *Ratios of Mo, V, and Al averaged from EDS data over 5 areas in each sample (the MAX phase, ML-MXene etched in HF-only, and the ML MXene etched in the HF/HCl mixture). Vanadium is normalized to 1 to simplify the relationship between Mo and V. "n.q" means "not quantifiable" in EDS. EDS data for the MXenes can be found in the Supporting Information (Supporting Information Fig. SI-6)*

	Rel. at. % (V normalized)		
Sample	**Mo**	**V**	**Al**
$(Mo_{0.75}V_{0.25})_5AlC_4$	2.7	1	1.1
ML-$(Mo_{0.75}V_{0.25})_5C_4$ (HF only)	3.32	1	n.q
ML-$(Mo_{0.75}V_{0.25})_5C_4$ (HF/HCl)	3.17	1	n.q

Exfoliation into MXene: $(Mo_{0.75}V_{0.25})_5C_4$

Once aluminum is removed from the MAX phase using hydrofluoric acid (HF), the sheets are separated (Figure 4 b) and the multilayered MXene powder is collected, which can be delaminated further into single- and few layered-MXene nanosheets. After removal of the Al, the *M-X* layers of the MXene structure are expected to be similar to those of the parent MAX phase, so we expect each layer will also have the herringbone structure seen above.

Figure 6 shows the XRD data of the MAX phase as well as the multilayered (ML-) and delaminated (D-) respective MXenes using HF and HF/HCl, from 0-30 °2θ as well as in the low diffraction angle region (up to 5 deg). Etching the sample with either etchant (HF or HF/HCl) leads to the removal of the Al layers leaving van-der-Waals-stacked ML-MXenes. This transformation can be followed in the X-ray diffraction data (Figure 6) where the intensity of most MAX phase peaks (except for the (110) peak) decreases significantly upon treatment with the etchants (HF: red line, HF/HCl: dark blue line). As observed for other MAX-to-MXene transitions, the (002) peak broadens and shifts to lower diffraction angles corresponding to a larger c-lattice parameter (c-LP) due to M_6X layers separating as the Al is removed.

The (002) reflection for the ML-MXene that was etched with HF only is found at 1.527 °2θ, which corresponds to a *d*-spacing of 17.223 Å and a c-LP of 34.446 Å. Once delaminated, the reflection shifts to 1.446 °2θ, which has a *d*-spacing of 18.190 Å and a c-LP of 36.380 Å. The (002) reflection of the multilayered sample etched with the mixture of HF and HCl is found at 1.446 °2θ, which means that the *d*-spacing is 18.190 Å and the c-LP is 36.380 Å. The delaminated sample in this case shifts slightly higher to 1.452 °2θ, with a *d*-spacing of 18.113 Å and a c-LP of 36.226 Å. In both cases, this is significant downshift from the original MAX phase (002) reflection at 1.8797 °2θ (*c*-LP: 27.9813(3) Å), indicating that the unit cell has expanded upon removal of the *A* element. Deysher *et al.* report a c-LP of 36.0 Å for multilayered products,[18] and the HF/HCl etched sample agrees with that result.

We note that the (002) peak in the XRD data of the HF-etched ML-MXene (dashed grey line in Figure 6) has a smaller shift to lower diffraction angles than the respective peak of the samples produced with HF/HCl as the etchant. This is likely the result of the different etching times (8d in the case of HF-etching versus 12d in the case of HF/HCl etching) leading to a more significant separation of the $(Mo_{1-x}V_x)_5C_4$ layers when the exfoliation time was four days longer. However, after delamination, both D-MXene samples show a similar peak position of the (002) reflection (orange and light blue line in Figure 6) indicating the presence of mostly delaminated nanosheets. The only difference is a more pronounced broadening of the (002) peak in the case of the D-MXene produced with HF (orange line in Figure 6). This implies that the latter MXenes are laterally smaller in size, which can be correlated with DLS measurements (*Supporting Information Fig. SI-7*). This is likely due to the harshness of the HF treatment, where concentrated HF is used to remove aluminum from the structure but can also etch transition metals from the surface and edges. The addition of HCl reduces the HF concentration to 30%, and prior research has shown that chloride ions are also possible etchants in the exfoliation process.[34] The addition of HCl also means that Cl^- will be an additional terminating group, as seen in the EDS (*Supporting Information Fig. SI-6*) and XPS data (*Supporting Information Fig. SI-10a*).

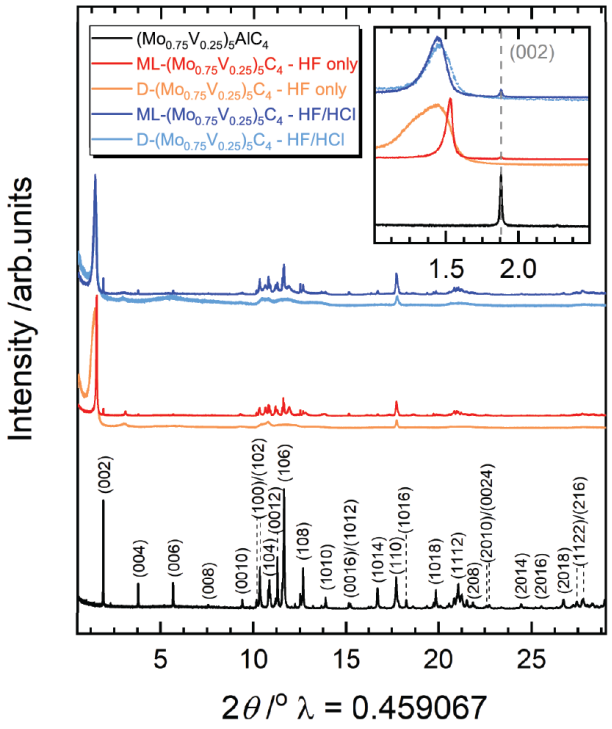

Figure 6: X-ray powder diffraction data of the precursor MAX phase (black), multilayer (ML-) MXene produced with HF (red) vs ML-MXene produced with a mixture of HF and HCl (dark blue), as well as the respective delaminated (D-) MXene samples (orange and light blue, respectively). Major (*hkl*) values have been included to demonstrate how reflections shift as the sample undergoes etching and delamination. (Note: not all (*hkl*) markers are listed). Reflections with two hkl values listed are in order from lower °2θ to higher °2θ. The inset reveals the shift of the (002) reflection as well as its peak shape depending on the etchant.

The disordered nature of the MXenes, especially the delaminated MXenes, makes it difficult to analyze their atomic structure using classic crystallographic techniques such as XRD. For these so-called "crystallographically challenged" materials, PDF is a powerful method to investigate their atomic structure.[35,36] Figure 7 compares the PDFs obtained from the two multilayered and two delaminated MXenes alongside the PDF obtained from the "514" MAX phase. The PDFs are all very similar, indicating no major differences between the local structure of the MAX phase and the MXenes. As a simple model, we use the crystal structure model of the "514" phase also used in Figure 3. This model returns a good fit of especially the multilayered MXenes (Figure 8, *SI-4f*), but also of the delaminated MXenes (*Supporting Information Fig. SI-4e*). The refined structures expand along the crystallographic c-axis from around 28 Å to around 29 Å which match the removal of Al and much less coherence between the individual Mo/V-C layers. This does not match the observed d-spacings in the XRD data, but it is acceptable, as this model should not be taken as the "true" crystal structure of the MXenes. Instead, it is a very simple model that can explain the structural features of the MXenes.

The PDFs show that the structure of the MXenes obtained from $(Mo_{0.75}V_{0.25})_5AlC_4$ is essentially the molybdenum/vanadium carbide layers from the parent MAX phase. Closer inspection of the PDFs obtained from the delaminated MXenes show at least 3 distinct distances between 1.5 and 2.5 Å. In the MAX phase, only one interatomic distance, the metal to carbon bond (~2.1 Å), should be present in this region. Instead, two extra peaks at 1.71 and 2.34 Å are observed. The Inorganic Crystal Structure Database was used to search for possible matches for these interatomic distances. The peaks at 1.71 Å and 2.34 Å could both be V-F and Mo-F distances, as these environments are also observed in the HAXPES measurements. In the MXenes processed in the HF/HCl solution the peak at 2.34 Å also matches well with a Mo-Cl and V-Cl distance. These distances show that the F and Cl are bonded directly to Mo and V.

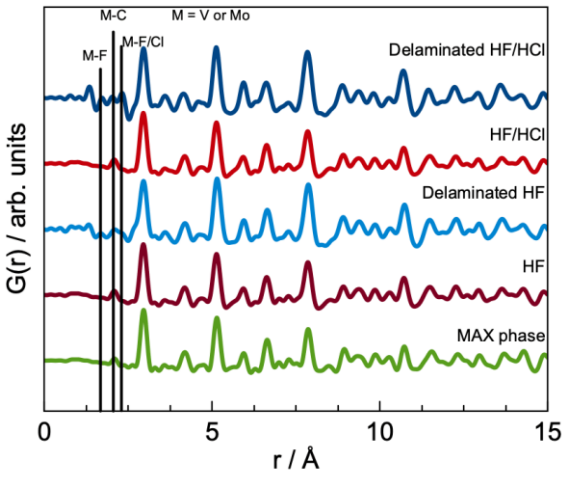

Figure 7: *PDF data for $(Mo_{0.75}V_{0.25})_5AlC_4$ (green) and the $(Mo_{0.75}V_{0.25})_5C_4$ MXene etched (brown) and delaminated (light blue) in HF, as well as the same MXene etched (red) and delaminated (dark blue) in an HF/HCl mixture. Local bonding data is marked with black lines to represent bonding between the M element and carbon or terminating groups.*

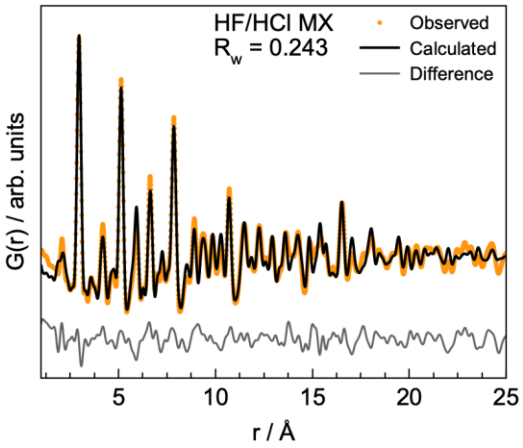

Figure 8: *Real-space Rietveld refinement of HF/HCl etched MXene fit with P-6c2 model for $(Mo_{0.75}V_{0.25})_5AlC_4$, where the Al occupancy is set to 0, with orange dots representing experimental PDF, a black and grey line showing the calculated PDF and difference curve, respectively.*

STEM-in-SEM

Figure 9 a shows a marginal bright-field image of MXene flakes exfoliated with HF/HCl on an ultrathin carbon support film. Numerous flakes are visible, including predominantly monolayers overlapping in various orientations. The MXene sample exfoliated with HF-only exhibited a similar appearance. Figure 9 b and Figure 9c show the diffraction patterns averaged over region 1 (monolayer thickness) and region 2 (bilayer thickness), respectively, as indicated in Figure 9 a. Note that for this 4D dataset, a beam convergence semi-angle of approximately 3.5 milliradians was used to produce easily observable diffraction spots. Both diffraction patterns are representative of hexagonal crystal structure. Kinematically forbidden reflections in Figure 9 c can all be attributed to double diffraction from two monolayers rotated by 24 degrees with respect to each other about the [001] axis. Different flakes can be observed/identified by selecting specific reflections to create virtual dark-field images. For example, Figure 9d shows a dark-field image comprising regions of the sample that scatter electrons into the 6 diffraction spots highlighted in red in the inset diffraction pattern. Part of a single large flake and several smaller flakes are visible.

Figure 10 shows ring diffraction patterns obtained using quasi-parallel illumination, rastering the electron beam over numerous grains in random orientations and using a 30 second camera integration time. Here, the beam convergence angle was approximately 1 milliradian which was obtained using a 7.5 mm diameter electron beam-limiting aperture and focusing the beam approximately 20 mm under the sample. The inset diffraction pattern was obtained from the exfoliated HF/HCl MXene sample, and the inset red arcs indicate different reflections. Ring diffraction patterns were obtained from both exfoliated HF and HF/HCl MXenes and then integrated azimuthally to obtain the curves shown in Figure 10. Based on the (100), (110), and (200) reflections, the a-lattice parameters for both samples were calculated and are indicated in the figure. Experimentally, the a-lattice parameter obtained from the exfoliated MXene samples are practically identical (i.e., approximately 2.972 Å) and are in excellent agreement with high-resolution XRD results obtained from the MAX phase samples.

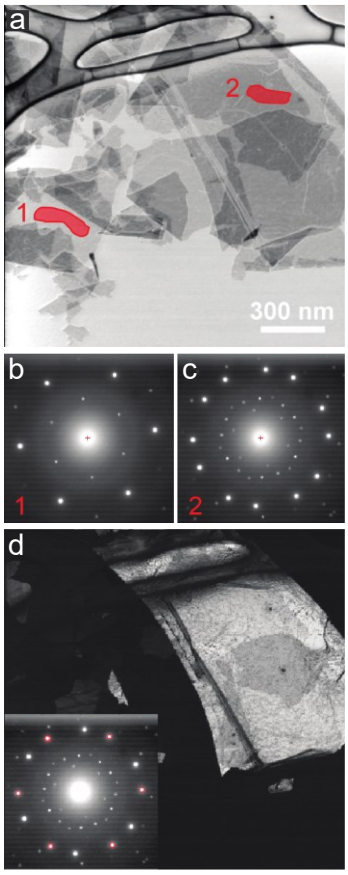

Figure 9: *(a) A marginal bright-field image obtained from a 4D dataset showing exfoliated MXene flakes prepared using HF/HCl. Diffraction patterns in (b) and (c) were obtained from the regions highlighted in red in (a). (d) A dark-field image using the virtual aperture indicated by the red circles in the inset diffraction pattern. A video of 4D-STEM over the MXene flakes can be found in Supporting Information (online).*

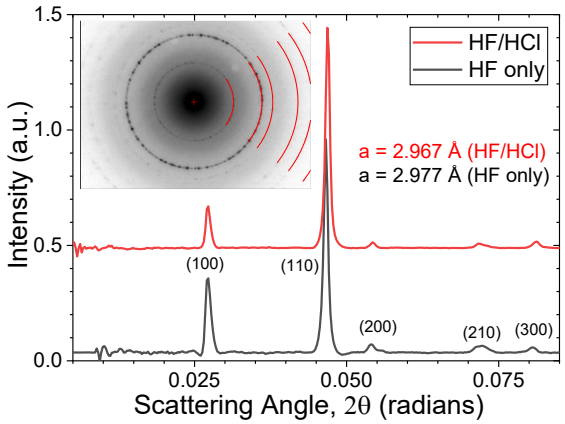

Figure 10: *Azimuthally-integrated diffraction patterns of exfoliated MXenes obtained in the SEM at 30 keV. The inset image shows a ring diffraction pattern with several reflections indicated by red arcs, and the a-lattice parameters for both MXene samples are shown.*

X-ray Photoelectron Spectroscopy (XPS)

Using laboratory-based SXPS measurements, a surface-sensitive elemental quantification was also obtained. In good agreement with the EDS quantification listed in Table 1, the SXPS Mo:V atomic ratio of the multilayered MAX phase etched in HF only and HF/HCl (ML-MXene) were determined to be 3.2:1.0 and 3.1:1.0, respectively. This result indicates that the Mo:V ratio is consistent from the surface to the bulk of the samples. Additionally, the Mo:V and Al:V ratio of the MAX-phase was determined to be 2.4:1 and 1.4:1, respectively, again, in good agreement with the EDS-determined ratio. See *Table SI-9* for the complete SXPS elemental quantification values.

Photoelectron spectroscopy (PES) provides information on the chemical state of the samples. The SXPS and HAXPES survey spectra displayed in *Figures SI-9* and *SI-10*, respectively, show that all samples are of high purity with the expected signals from Mo, V, Al, C, F and O all present, along with minor contaminant traces of Ca, Si and Cl. Figure 11 shows the four main core level spectra of all samples in the 514 Mo-V-Al-C system collected using SXPS ($h\nu$ = Al Kα) and HAXPES ($h\nu$ = 5.9 keV). The equivalent figure comparing the spectra collected with SXPS ($h\nu$ = 1.7 keV) and HAXPES ($h\nu$ = 5.9 keV) at beamline I09 can be found in *Figure SI-10*. The MAX-phase core level spectra collected with HAXPES are not included due to charging effects during the measurements leading to distortion of the core level peaks (*Supporting Information Fig. SI-11*).

The difference in probing depth between SXPS and HAXPES arising from the difference in X-ray energy and, therefore, the kinetic energy of the photoelectrons allows for an evaluation of the chemical states present in the samples at both the surface and in the bulk. Using molybdenum carbide (MoC) as a simplified model for the MAX and MXene samples and recalling that the probing depth equates to three times the IMFP, the QUASES software package calculates the maximum probing depth in MoC at photon energies of 1.4867 and 5.9267 keV to be 7.3 and 22.1 nm, respectively.

The main difference between the MAX-phase and the MXenes is that metal oxide environments dominate the MAX-phase, whilst the MXenes (both etched and delaminated) mainly show environments related to a metallic character. This is particularly evident in the Mo 3*d* core level spectra displayed in Figure 11a. The Mo 3*d* spectra show that for the MXene samples, the main $3d_{5/2}$ peaks are located at low BEs and are split into two distinct environments at 228.2 and 228.8 eV. The peaks display a narrow full width at half maximum (FWHM) with some asymmetric character, typical for metallic systems. Based on the 0.6 eV energy separation and the line shape of the peaks, they are unlikely to arise from molybdenum carbide (Mo-C) and low valence state (i.e., 4+) molybdenum oxide (Mo-O) environments, but rather are attributed to two metallic environments. On the basis of the findings from the structural characterization, these peaks are attributed to Mo-rich and V-rich Mo/V-C environments, with the latter attributed to the lowest BE peak, owing to the lower electronegativity of V compared to Mo. This lower BE peak is also enhanced with HAXPES, aligning with the structural characterization results in that Mo is situated toward the outermost layers. The metallic nature of the MXenes is further reflected in the valence band spectra, which show a distinct Fermi energy (E_F) cut-off and large density of states at the Fermi energy (*Supporting Information Fig. SI-12c*).

In contrast to the MXene samples, the Mo 3*d* spectrum of the MAX-phase collected with SXPS (red line) is dominated by features at significantly higher BEs (≈231.8 and 234.7 eV) commensurate with Mo(VI) oxide (labelled as Mo-O).[37] A low intensity and low BE peak is present in the Mo 3*d* SXPS spectrum of the MAX-phase sample (red line) and is attributed to a

Mo/V/Al-C environment. A small amount of Mo(VI) oxide is also present for multilayer and delaminated MXene samples, with the multilayered samples exhibiting a slightly greater intensity of the oxide than the delaminated ones. The choice of HF or HF/HCl has minimal effect on the Mo chemical state of the MXene observed with XPS. The high level of oxidation in the MAX phase sample may arise from the presence of Al and the metals' high affinity to adsorb atmospheric oxygen. The Al 2*s* spectra collected with SXPS/HAXPES are displayed in Figure 11b. Al only appears to be present with significant intensity in the MAX phase, with the SXP spectra showing a single, broad peak at 118.6 eV, commensurate with an aluminum oxide environment.[38] A very low-intensity Al peak is found in the HAXPES data (see magnified inset in the Figure), agreeing well with the EDS results in that the etching procedure successfully removes the majority, but not all, of the Al.

The V 2*p* core level spectra collected with both SXPS and HAXPES are presented in Figure 11c. They show a typical asymmetric doublet peak shape for the MXene samples with the V $2p_{3/2}$ peak positioned at 513.2 eV and a spin-orbit splitting of 7.6 eV, commensurate with a metallic V-C environment.[39] The spectrum of the MAX-phase is strikingly different, with an absence of sharp asymmetric peaks and, instead, a dominance of higher BE features on either side of the V-C V $2p_{1/2}$ peak attributed to metal oxide environments (V-O). Much like the Mo 3*d* spectra the etched samples, more so than the delaminated, display a minor contribution from V-O environments. In all V 2*p* spectra, the Mo 3*s* core line is present on the lower BE side (≈507.0 eV). Between the SXPS and HAXPES data a change in the V2*p*/Mo 3*s* peak intensity is evident. However, this is due to the differences in decay rates of the photoionization cross sections of the two core levels when increasing the X-ray photon energy rather than a change in the transition metal ratio.

The C 1*s* core level spectra are displayed in Figure 11d. Multiple carbon environments are observed for all samples. In particular, a clear lower BE peak with strong intensity at ≈282.9 eV is observed for the MXene samples with both SXPS and HAXPES. This peak arises from the metal-carbide (C-Mo/V) environment present, and its intensity relative to the adventitious carbon environment (C^0) becomes enhanced with HAXPES. Owing to the increased probing depth of HAXPES, this change in relative intensity indicates a greater presence of C-Mo/V species in the bulk of the samples. Comparing the multilayered to the delaminated samples, the latter shows a greater carbide to C^0 ratio. All samples also display varying amounts of C-O and O-C=O environments towards higher BEs. These environments are also reflected in the O 1*s* spectra (*Supporting Information Fig. SI-12a*). However, these environments contribute little to the O 1*s* spectra as it is dominated by the metal-oxide signal at ≈530 eV.

The F 1*s* spectra collected with SXPS (*Supporting Information Fig. SI-12b*) show two environments, an intense peak at ≈684.0 eV and a low-intensity peak at ≈688.2 eV for the MXene samples with no F detected in the MAX phase as expected. The two environments are attributed to metal fluoride (M-F_x) and C-F_x environments with the M-F environments dominating.[40,41]

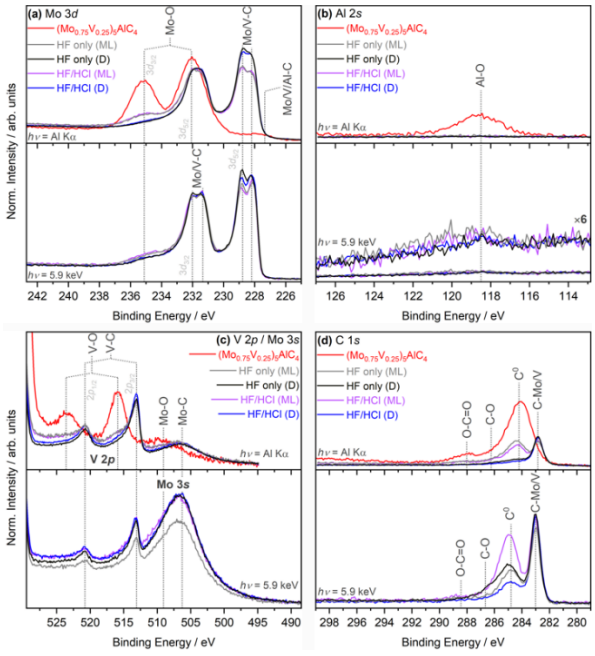

***Figure. 11**: SXPS (hν = Al Kα) and HAXPES (hν = 5.9 keV) data of samples in the 514 Mo-V-Al-C system, including the (a) Mo 3d, (b) Al 2s, (c) V 2p/Mo 3s, and (d) C 1s core levels. The sub figures contain two panels with the top and bottom panels displaying the SXPS and HAXPES data, respectively. (ML) and (D) refer to the multilayered and delaminated MXene sample sets, respectively. In subfigure (b) a ×6 magnified inset is included to aid viewing of the low intensity Al 2s peaks. The MAX-phase spectra collected with HAXPES are not shown here due to charging but are included in Supplementary Information (Supporting Information Fig. SI-12).*

Electrochemical Measurements

Due to MXenes' good electronic conductivity and because the hydrogen evolution reaction is such a high-interest subject,[42–44] the application of this MXene as a potential catalyst for hydrogen reduction is being assessed here.

The anodic linear sweep voltammograms were collected for both samples, for an initial run as well as after cycling 50 times. Figure 12 shows the linear sweep voltammograms for each sample before and after they are cycled to determine their overpotential at 10 mA cm^{-2}. The $(Mo_{0.75}V_{0.25})_5C_4$ MXene etched with only HF shows surprising results, where the initial run reached an overpotential of 754 mV at a current density of 10 mA cm^{-2} and, after cycling 50 times, the overpotential decreased to 166 mV. The Tafel slopes show a similar trend, with the initial measurement at 154.1 mV dec^{-1} and after 50 cycles, 73.7 mV dec^{-1}. Why this happens is unclear, but repeated experiments showed similar results. Surface terminations on the HF-only sample likely play a big part. In a previous study of another MXene, V_4AlC_3, we hypothesized that -O terminating surface species that are etched away during cycling are responsible for the change in the electrochemical behavior.[45] The sample etched in the HF/HCl mixture initially had an overpotential of 512 mV at 10 mA cm^{-2} and after 50 cycles, the overpotential reduced to 425 mV. The Tafel slopes for the initial and 50 cycle runs were 322.6 mV dec^{-1} and 306.0 mV dec^{-1}, respectively. While the HF/HCl samples were not as effective as the HF only sample after cycling, they are more stable and have a better initial overpotential. For comparison, one of the ideal HER catalysts, Pt/C (20%), has an overpotential of roughly 48 mV at 10 mA cm^{-2} and a Tafel slope of 30 mV dec^{-1}.[46] The HF/HCl MXene is also comparable to other species, such as Mo_2C MXene, which has an overpotential of 305 mV at 10 mA cm^{-2} after cycling 30 times,[25] V_4C_3, with an overpotential of 200 mV at 10 mA cm^{-2},[47] and Ti_3C_2 nanofibers with an overpotential of 169 mV at 10 mA cm^{-2}.[26]

Further investigation into the electrocatalytic properties and the stability of these MXenes is needed to fully assess their potential as electrocatalysts for the hydrogen evolution reaction.

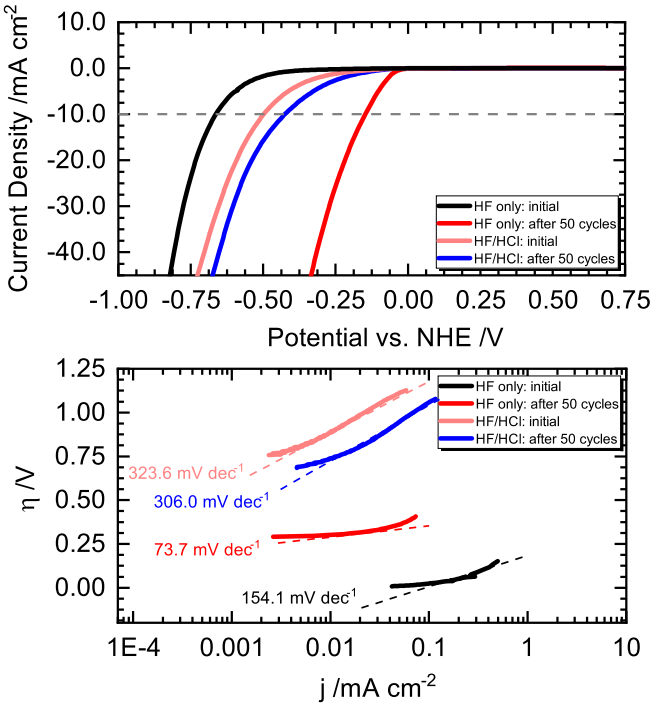

Figure 12: *(top) Linear sweep voltammograms for hydrogen reduction comparing results between initial sweeps of HF- only etched (black) and HF/HCl etched (pink) samples as well as the same samples after 50 cycles (red and blue, respectively. A grey dashed line is used to illustrate a current density of 10 mA cm^{-2}. These samples were collected with a scan rate of 20 mV s^{-1} in 0.5 M H_2SO_4 (bottom) Tafel slopes for the same samples taken from linear sweep results. All samples use corresponding colors for simplicity.*

Conclusions

We provide further details on the synthesis and structure of the "514" MAX phase $(Mo_{0.75}V_{0.25})_5AlC_4$ and its MXene sibling. Unlike published results, the addition of an oxide was not necessary for the MAX phase to form in our laboratory, yet the reaction mixture had to be heated at 1,600 °C three times. The product contains an unknown side phase as well as (potentially Mo-doped) V_4AlC_3. The high quality of the main product was confirmed by synchrotron X-ray diffraction data and pair distribution analysis. The structure has been found to differ from the typical MAX phase structure that crystallizes with space group $P6_3/mmc$. Our refinements suggest $(Mo_{0.75}V_{0.25})_5AlC_4$ to adopt space group $P\text{-}6c2$ which is closely related to the reported one ($P\text{-}6m2$). Due to uncertainties regarding the refinements of the diffraction data of the product at hand (small amounts of multiple side

phases), further analysis is necessary to fully confirm the space group of the 514 MAX phase (ideally performed on a single crystal of $(Mo_{0.75}V_{0.25})_5AlC_4$, for example). The diffraction as well as spectroscopy (EDS, XPS) data show that the MAX phase is a solid solution with a Mo:V ratio of 3:1 (different from the initially reported ratio of 4:1).

We use two different methods to etch the solid-solution "514" MAX phase into the respective MXene, one using only HF and one using a mixture of HF and HCl. XPS and 4D STEM-in-SEM give further insight into the MXene structure and surface terminations, which is affected by etchant selection. With the addition of HCl in the etching solution, Cl^- ions are present on the surface of the MXene. This affects the stability of the MXene as a potential catalyst for HER, with overpotentials of 166 mV (HF-only) and 425 mV (HF/HCl) after cycling in 0.5 M H_2SO_4 solution.

Materials and Methods

Synthesis of $(Mo_{0.75}V_{0.25})_5AlC_4$: Elemental powders of molybdenum (Thermo Fisher -325 mesh, 99.99%), vanadium (Alfa Aesar, -325 mesh, 99.50%), aluminum (Alfa Aesar, -325 mesh, 99.50%), and graphite (Alfa Aesar, -325 mesh, 99.9995%) were weighed in a glovebox under an argon (Ar) atmosphere. To synthesize approximately 5 g of $(Mo_{0.75}V_{0.25})_5AlC_4$, 3.582 g Mo (3 mol), 0.634 g V (1 mol), 0.504 g Al (1.5 mol) and 0.404 g C (2.9 mol) were mixed using a ball mill (Retsch, MM400, WC grinding jar, 2 10 mm WC balls) for 5 minutes at a rate of 25 s^{-1}. Once thoroughly mixed, the powder was pressed using a 13 mm die (Specac) under 5 T of pressure in a hydraulic press (Specac, Atlas 15T). The resulting pellet was then heated in a tube furnace (alumina crucible inside Carbolite Gero) for 6 h at 1600 °C with a heating rate of 5 °C min^{-1} under a flowing Ar atmosphere (50 cc min^{-1}). Once the sample had passively cooled to room temperature, it was crushed in a mortar and repressed into a pellet using the above specifications. The sample was heated again at 1600 °C for 6 h under the same conditions, and was then crushed, pressed, and annealed one final time. After the third heating step, the MAX phase product was collected in the form of a pellet and crushed with a mortar and pestle for subsequent exfoliation and further analysis. X-ray diffraction data of the product obtained after each heating step are shown in the Supporting Information (*Supporting Information Fig. 5*). Please note that the 3:1 ratio of Mo:V corresponding to the chemical composition $(Mo_{0.75}V_{0.25})_5AlC_4$ was necessary for successful MAX phase synthesis. The reported 4:1 Mo:V ratio[16] leads to a product that mostly decomposed after the second heating step (*Supporting Information Fig. SI-13*).

Synthesis of $(Mo_{0.75}V_{0.25})_5C_4$ – HF only method: HF-based exfoliation of $(Mo_{0.75}V_{0.25})_5AlC_4$ is reproduced from Deysher *et al*.[18] A Teflon beaker with a Teflon stir bar containing 20 mL of hydrofluoric acid (HF; VWR, 48-50%) was immersed in an ice bath prior to addition of the MAX phase. Once cooled, 1 g of powder sample was added to the beaker over 5 minutes, preventing thermal runaway. The mixture was allowed to stir for 5 minutes before being removed from the ice bath and added to an oil bath. The oil bath was heated to 35 °C and the sample was set to react with mixing at 50 RPM over 8 d (192 h). Once etching was complete, the mixture was washed with water using a centrifuge (Eppendorf centrifuge 5810) at 3500 RPM for 5 minutes to remove excess HF until the solution was neutral (~5-6 washes). The resultant multilayer (ML-) MXene powder was filtered through a PVDF filter (Millipore Sigma) and dried under ambient conditions for further analysis and delamination.

Synthesis of $(Mo_{0.75}V_{0.25})_5C_4$ – HF/HCl method: The sample was prepared in the same way as the above method with a few key changes: The etching solution was a mixture of 8 mL hydrochloric acid (HCl; VWR, 70%) and 12 mL HF (VWR, 48-50%) for 1 g of MAX phase and once moved into the oil bath, the sample was left to react for 12 d (288 h) before washing and collecting the ML-MXene. Note the longer reaction time is necessary because this acid mixture is less aggressive than pure HF.

Delamination of $(Mo_{0.75}V_{0.25})_5C_4$: In a 20 mL glass vial, 0.5 g of ML-MXene and 20 mL of 5% tetrabutylammonium hydroxide (TBAOH, Fisher Scientific) were added, along with a stir bar. The sample was left to stir at a rate of 200 RPM for 18 h. Once finished, the sample was washed and centrifuged at 3500 RPM for 10 minutes until it was neutral (~2 washes). Once the solution was neutral, the black, colloidal delaminated (D-) MXene supernatant was collected after each centrifugation until the solution became transparent. The colloidal solution was further centrifuged (Thermo Scientific,

Sorvall Lynx 4000) at 10000 RPM for 45 minutes to concentrate the D-MXene into a solution of ~7.5 mg/mL. The ink was then diluted as needed to make a filtered $(Mo_{0.75}V_{0.25})_5C_4$ film and electrode films.

Laboratory X-Ray diffraction measurements: All products were structurally characterized by X-ray powder diffraction (Bruker D2 Phaser, 2nd Generation) in Bragg-Brentano geometry, equipped with a Cu-K_α X-ray source (λ = 1.5406 Å), and a LYNXEYE 1D SDD detector. Powder samples were loaded onto a silicon wafer and inserted into a sample holder. All measurements were performed over a range of 0.5-90 °2θ with a step scan of 0.05 °2θ, and dwell time of 1.5 s per step.

Synchrotron X-ray diffraction measurements: High-resolution powder diffraction data were collected at beamline 11BM at the Advanced Photon Source (APS), Argonne National Laboratory, using an average wavelength of 0.459067 Å. Discrete detectors covering an angular range from -6 to 16 °2θ are scanned over a 34 °2θ range, with data points collected every 0.001 °2θ and a scan speed of 0.01 °/s. The 11-BM instrument uses X-ray optics with two platinum-striped mirrors and a Si(111) double crystal monochromator, where the second crystal has an adjustable sagittal bend.[48] Ion chambers monitor incident flux. A vertical Huber 480 goniometer, equipped with a Heidenhain encoder, positions an analyzer system comprised of twelve perfect Si(111) analyzers and twelve Oxford-Danfysik $LaCl_3$ scintillators, with a spacing of 2 °2θ.[49] Analyzer orientation can be adjusted individually on two axes. A three-axis translation stage holds the sample mounting and allows it to be spun, typically at ~5400 RPM (90 Hz). A Mitsubishi robotic arm mounts and dismounts samples on the diffractometer.[50] An Oxford Cryosystems Cryostream Plus device allows sample temperatures to be controlled between 80-500 K when the robot is used. The diffractometer is controlled via EPICS.[51] Data are collected while continually scanning the diffractometer 2θ arm. A mixture of NIST standard reference materials, Si (SRM 640c) and Al_2O_3 (SRM 676) is used to calibrate the instrument, where the Si lattice constant determines the wavelength for each detector. Corrections are applied for detector sensitivity, 2θ offset, small differences in wavelength between detectors, and the source intensity, as noted by the ion chamber, before merging the data into a single set of intensities evenly spaced in 2θ. Rietveld refinement of 11-BM data was performed in GSAS-II[52] using a $(Mo_{0.75}V_{0.25})_5AlC_4$ crystallographic file modeled in VESTA to fit the high-resolution data.

Pair Distribution Function (PDF) analysis: The total scattering pattern was obtained from 11-ID-B at the Argonne National Laboratory of the APS using X-rays with a photon energy of 86.7 keV (l = 0.143 Å) as part of the mail in program. The total scattering was obtained using the rapid acquisition PDF method[53] where a 2D detector is placed close to the sample. In this case a Perkin Elmer 1621 detector was placed 180 cm from the samples and a flat field correction was applied to the acquired images. The sample-to-detector distance was calibrated using a CeO_2 standard. The 2D data were integrated using Dioptas,[54] and the 1D total scattering patterns were Fourier transformed to obtain the Pair Distribution Function (PDF) using PDFgetX3[55] in the program XPDFsuite.[56] The PDF was Fourier transformed from 0.7 – 24 $Å^{-1}$. The powders were loaded into Kapton capillaries and the scattering from an empty Kapton tube was used for background subtraction. The obtained PDFs were analyzed using PDFgui.[57] The scale factor, unit cell, atomic positions, isotropic atomic displacement factors, and the correlated motion parameter, d_2, were refined. The instrument parameters Q_{damp} and Q_{broad} were obtained using a CeO_2 standard.

Scanning Electron Microscopy and Energy Dispersive Spectroscopy: Powder and film samples were supported on an aluminum pin with carbon tape. The samples were then inserted into the Zeiss Auriga Focused Ion Beam/Scanning Electron Microscope using a 12-pin sample holder. The Zeiss Auriga employed a Ga liquid metal ion source in combination with a high-resolution Gemini field Emission SEM column with a Schottky thermal field emitter to image samples at 5 keV using an in-lens detector. All micrographs were formatted using the ImageJ software package.[58] A Chamber-Everhart-Thornley secondary electron detector and Oxford X-Max were used to collect EDS measurements using a 10 keV accelerating voltage. All data were collected using AZtec.

Scanning Transmission Electron Microscopy:

Multilayered MXene powder samples were dispersed in ethanol (Decon Labs, 95%) (5 mg/1 mL) and sonicated for 30 minutes and the resulting solution was drop cast onto a lacey carbon TEM grid. Samples were analyzed using the JEOL ARM200F aberration-corrected STEM with a Schottky field emission gun after leaving the samples under vacuum for 8 h. A 200 keV acceleration voltage was used to collect micrographs and Gatan software was used to collect data which was further formatted using ImageJ.[58]

4D STEM-in-SEM: MXene samples were diluted from stock solution 1:500 in ultrapure water and deposited on TEM grids with ultrathin carbon films. SEM and 4D STEM-in-SEM was performed on a Zeiss Gemini 300 field emission scanning electron microscope at 30 keV. The experimental set-up for 4D STEM-in-SEM is described in detail by Caplins et. al.[59] Briefly, electrons are transmitted through the sample to strike a phosphor screen, which emits photons. The resulting optical diffraction pattern is imaged out of the SEM vacuum chamber onto a CCD camera. In-house developed software was used to analyze data.

Soft and hard X-ray photoelectron spectroscopy (SXPS/HAXPES) measurements: SXPS and HAXPES measurements at photon energies of 1.744 and 5.927 keV, respectively, were performed at beamline I09 of the Diamond Light Source.[60] These photon energies will be referred to as 1.7 and 5.9 keV in the remaining manuscript for simplicity. The soft X-ray photon energy was obtained using a 400 lines/mm plane grating monochromator, whereas a Si(111) double crystal monochromator in conjunction with a Si(004) post-channel-cut monochromator was used to obtain the hard X-ray energy. The total energy resolution of the SXPS and HAXPES measurements was determined by extracting the 16/84% width of a Fermi edge of a polycrystalline gold foil and was found to be 410 and 280 meV, respectively. The end station operates under a base pressure of $3x10^{-10}$ mbar and is equipped with a VG Scienta EW4000 high-voltage electron analyzer. Samples were mounted on adhesive, conducting carbon tape. Due to the set-up of the beamline, SXPS and HAXPES measurements were performed on the same sample and on the same spot of the sample. Both SXPS and HAXPES measurements were performed using near-normal emission geometry. Survey, key core level (Mo 3*d*, V 2*p*, Mo 3*s*, C 1*s*, Al 2*s*, and O 1*s*) and valence band spectra were measured for all samples at both photon energies. The Al 2*s* was selected over the Al 2*p* because the latter overlaps with the Mo 4*s* / V 3*s* region. Additional laboratory-based SXPS measurements were performed on a Thermo Scientific K-Alpha XPS system to obtain elemental quantification of the samples. The samples were prepared in the same manner as the synchrotron-based SXPS/HAXPES measurements. This spectrometer consists of a 1.4867 keV (Al Kα) monochromated photon source, 180° double-focusing hemispherical analyser, 128-channel detector, and a dual-source charge-compensating flood gun. The system operates under a base pressure of $9.8x10^{-9}$ mbar, and a 400 μm spot size was used. Survey spectra were collected at a pass energy of 200 eV, whereas the key core level and valence band spectra were collected at 20 eV. The total energy resolution of the spectrometer at a pass energy of 20 eV was determined to be 450 meV. The elemental quantification extracted from the core level spectra was conducted using the Thermo Scientific Avantage Data System software package (v5.9925). The relativistic inelastic mean free path (IMFP) was used to provide an estimate for the probing depth differences between the SXPS and HAXPES measurements. The IMFP values are calculated using the QUASES software package[61] that implements the Tanuma, Powell, and Penn (TPP-2M) predictive IMFP formula. All SXPS/HAXPES spectra are normalized to the total Mo 3*d* area. The binding energy (BE) scale of all spectra is calibrated to the intrinsic Fermi Energy (E_F) of each sample extracted from the valence band spectra.

Zeta potential and Dynamic Light Scattering (DLS): D-MXenes were diluted to 0.02 mg/mL and poured into zeta potential cuvettes, which were placed into the Malvern Zetasizer – Nano series. Zeta potential measurements were averaged over ten runs per trial, with three total trials. The same sample was then poured into a polystyrene cuvette for DLS, using the same instrument. The measurements were taken with an average of ten runs per trial for a total of three trials.

Electrochemical measurements: All electrochemical measurements were performed with reference to the methods used by Seh *et al.*[25] A solution consisting of 0.5 mg of ML-MXene powder, 5 µL of Nafion *D-520 solution (5% w/w), and 100 µL of ethanol (Decon, 95%) were sonicated for 30 minutes. The solution was drop

cast onto a 5 mm glassy carbon electrode disc for a mass loading of 0.1 mg/cm^2 and left to air dry overnight. The electrode was then placed on a rotator and inserted into a 3-electrode cell (Metrohm) with a platinum counter electrode and Ag/AgCl reference electrode. The electrolyte solution was 0.5 M sulfuric acid (H_2SO_4) (VWR, 95-98%) that had been bubbled with argon for 1 hour to remove oxygen. The working electrode was rotated at 1600 RPM to reduce the formation of bubbles at the electrode surface. Linear sweep voltammetry was done with a scan rate of 20 mV s^{-1}, using a Squidstat Potentiostat. Cyclic Voltammetry was also employed to remove surface impurities from the electrode and measure stability up to 50 cycles. No iR correction was applied.

Acknowledgments
This material is based upon work supported by the National Science Foundation under Grant No. 2143982. 4D STEM: Partial contribution of the US Government. Not subject to copyright in the United States. Use of the Advanced Photon Source at Argonne National Laboratory was supported by the U. S. Department of Energy, Office of Science, Office of Basic Energy Sciences, under Contract No. DE-AC02-06CH11357. The mail-in program at Beamline 11-ID-B and 11-BM contributed to the data. A special thank you to J. Weng, U. Rhett, and the staff at Argonne National Laboratory for their assistance.
C.K. and A.A.R acknowledge the support from the Department of Chemistry, UCL. A.R. acknowledges the support from the Analytical Chemistry Trust Fund for her CAMS-UK Fellowship. We acknowledge Diamond Light Source for time on Beamline I09 under Proposal NT29451-6.

Supporting Information
Crystallographic data including crystallographic information framework (CIF) files; Synchrotron X-ray pattern for unknown phase; Space group comparison of synchrotron X-ray data; Pair distribution function analysis from synchrotron X-ray source for *ex-situ* MAX phase measurements and MXenes; *ex-situ* laboratory X-ray diffraction data; EDS data for MXenes; Zeta potential and DLS measurements for MXenes; Laboratory SXPS elemental quantification; Laboratory and synchrotron X-ray SXPS survey spectra; Laboratory and synchrotron X-ray SXPS core level spectra; Laboratory XRD data for alternate MAX phase synthesis technique

Conflict of interest
The authors have no conflicts to disclose.

Author Contributions
Rose M Snyder: Conceptualization (equal), Formal Analysis (equal), Visualization (lead), Investigation (equal), Writing – original draft (equal), Writing - review & editing (equal).
Mikkel Juelsholt: Formal Analysis (lead), Visualization (equal), Investigation (equal), Writing – original draft (equal), Writing - review & editing (equal).
Curran Kalha: Formal Analysis (equal), Visualization (equal), Investigation (equal), Writing – original draft (equal), Writing - review & editing (equal).
Jason Holm: Formal Analysis (lead), Visualization (equal), Investigation (equal), Writing – original draft (equal), Writing - review & editing (equal).
Elisabeth Mansfield: Formal Analysis (lead), Visualization (equal), Investigation (equal), Writing – original draft (equal), Writing - review & editing (equal).
Tien-Lin Lee: Formal Analysis (equal), Investigation (equal),
Pardeep K Thakur: Formal Analysis (equal), Investigation (equal),
Aysha A Riaz: Formal Analysis (equal), Investigation (equal),
Benjamin Moss: Formal Analysis (equal), Investigation (equal),
Anna Regoutz: Formal Analysis (lead), Visualization (equal), Investigation (equal), Writing – original draft (equal), Writing - review & editing (equal).
Christina S Birkel: Funding Acquisition (lead), Conceptualization (lead), Formal Analysis (equal), Visualization (equal), Investigation (equal), Writing – original draft (lead), Writing - review & editing (equal).

ORCid
Christina Birkel: 0000-0001-8979-5214
Rose M. Snyder: 0000-0003-2463-0966
Mikkel Juelsholt 0000-0001-6401-8267
Elisabeth Mansfield: 0000-0003-2463-0966
Curran Kalha: 0000-0002-3387-6880
Anna Regoutz: 0000-0002-3747-3763

Aysha A. Riaz: 0000-0003-0977-3651 Jason Holm : 0000-0001-9542-7979
Pardeep K. Thakur: 0000-0002-9599-0531

References

(1) Barsoum, M. W. The $M_{N+1}AX_N$ Phases: A New Class of Solids: Thermodynamically Stable Nanolaminates. *Prog. Solid State Chem.* **2000**, *28* (1–4), 201–281. https://doi.org/10.1016/S0079-6786(00)00006-6.

(2) Sokol, M.; Natu, V.; Kota, S.; Barsoum, M. W. On the Chemical Diversity of the MAX Phases. *Trends Chem.* **2019**, *1* (2), 210–223. https://doi.org/10.1016/j.trechm.2019.02.016.

(3) Barsoum, M.; El-Raghy, T. The MAX Phases: Unique New Carbide and Nitride Materials. *Am. Sci.* **2001**, *89* (4), 334. https://doi.org/10.1511/2001.28.736.

(4) Smialek, J. L.; Nesbitt, J. A.; Gabb, T. P.; Garg, A.; Miller, R. A. Hot Corrosion and Low Cycle Fatigue of a Cr_2AlC-Coated Superalloy. *Mater. Sci. Eng. A* **2018**, *711*, 119–129. https://doi.org/10.1016/J.MSEA.2017.10.098.

(5) Wang, K.; Du, H.; Wang, Z.; Gao, M.; Pan, H.; Liu, Y. Novel MAX-Phase Ti_3AlC_2 Catalyst for Improving the Reversible Hydrogen Storage Properties of MgH_2. *Int. J. Hydrogen Energy* **2017**, *42* (7), 4244–4251. https://doi.org/10.1016/J.IJHYDENE.2016.10.073.

(6) Grieseler, R.; Camargo, M. K.; Hopfeld, M.; Schmidt, U.; Bund, A.; Schaaf, P. Copper-MAX-Phase Composite Coatings Obtained by Electro-Co-Deposition: A Promising Material for Electrical Contacts. *Surf. Coatings Technol.* **2017**, *321*, 219–228. https://doi.org/10.1016/J.SURFCOAT.2017.04.060.

(7) Nowotny, V. H. Strukturchemie Einiger Verbindungen Der Übergangsmetalle Mit Den Elementen C, Si, Ge, Sn. *Prog. Solid State Chem.* **1971**, *5* (C), 27–70. https://doi.org/10.1016/0079-6786(71)90016-1.

(8) Barsoum, M. W.; Radovic, M. Elastic and Mechanical Properties of the MAX Phases. *Annu. Rev. Mater. Res.* **2011**, *41*, 195–227. https://doi.org/10.1146/ANNUREV-MATSCI-062910-100448.

(9) Sun, Z. M. Progress in Research and Development on MAX Phases: A Family of Layered Ternary Compounds. *Int. Mater. Rev.* **2011**, *56* (3), 143–166. https://doi.org/10.1179/1743280410Y.0000000001.

(10) Eklund, P.; Beckers, M.; Jansson, U.; Högberg, H.; Hultman, L. The $M_{n+1}AX_n$ Phases: Materials Science and Thin-Film Processing. *Thin Solid Films* **2010**, *518* (8), 1851–1878. https://doi.org/10.1016/J.TSF.2009.07.184.

(11) Wang, J.; Wang, J.; Zhou, Y.; Lin, Z.; Hu, C. Ab Initio Study of Polymorphism in Layered Ternary Carbide M_4AlC_3 (M = V, Nb and Ta). *Scr. Mater.* **2008**, *58* (12), 1043–1046. https://doi.org/10.1016/J.SCRIPTAMAT.2008.01.058.

(12) He, X.; Bai, Y.; Zhu, C.; Barsoum, M. W. Polymorphism of Newly Discovered Ti_4GaC_3: A First-Principles Study. *Acta Mater.* **2011**, *59* (14), 5523–5533. https://doi.org/10.1016/J.ACTAMAT.2011.05.025.

(13) Ashton, M.; Mathew, K.; Hennig, R. G.; Sinnott, S. B. Predicted Surface Composition and Thermodynamic Stability of MXenes in Solution. *J. Phys. Chem. C* **2016**, *120* (6), 3550–3556. https://doi.org/10.1021/ACS.JPCC.5B11887/SUPPL_FILE/JP5B11887_SI_001.PDF.

(14) Soomro, R. A.; Zhang, P.; Fan, B.; Wei, Y.; Xu, B. Progression in the Oxidation Stability of MXenes. *Nano-Micro Lett.* **2023**, *15* (1). https://doi.org/10.1007/S40820-023-01069-7.

(15) Lin, Z.; Zhuo, M.; Zhou, Y.; Li, M.; Wang, J. Microstructures and Theoretical Bulk Modulus of Layered Ternary Tantalum Aluminum Carbides. *J. Am. Ceram. Soc.* **2006**, *89* (12), 3765–3769. https://doi.org/10.1111/J.1551-2916.2006.01303.X.

(16) Zheng, L.; Wang, J.; Lu, X.; Li, F.; Wang, J.; Zhouw, Y. $(Ti_{0.5}Nb_{0.5})_5AlC_4$: A New-Layered Compound Belonging

To MAX Phases. *J. Am. Ceram. Soc.* **2010**, *93* (10), 3068–3071. https://doi.org/10.1111/J.1551-2916.2010.04056.X.

(17) Uddin, M. M.; Ali, M. A.; Ali, M. S. Structural, Elastic, Electronic and Optical Properties of Metastable MAX Phase Ti_5SiC_4 Compound. *Indian J. Pure Appl. Phys.* **2016**, *54* (6), 386–390. https://doi.org/10.56042/IJPAP.V54I6.4502.

(18) Deysher, G.; Shuck, C. E.; Hantanasirisakul, K.; Frey, N. C.; Foucher, A. C.; Maleski, K.; Sarycheva, A.; Shenoy, V. B.; Stach, E. A.; Anasori, B.; Gogotsi, Y. Synthesis of Mo_4VAlC_4 MAX Phase and Two-Dimensional Mo_4VC_4 MXene with Five Atomic Layers of Transition Metals. *ACS Nano* **2020**, *14*, 59. https://doi.org/10.1021/acsnano.9b07708.

(19) Mashtalir, O.; Naguib, M.; Mochalin, V. N.; Dall'Agnese, Y.; Heon, M.; Barsoum, M. W.; Gogotsi, Y. Intercalation and Delamination of Layered Carbides and Carbonitrides. *Nat. Commun.* **2013**, *4* (1), 1716. https://doi.org/10.1038/ncomms2664.

(20) Gogotsi, Y.; Anasori, B. The Rise of MXenes. *ACS Nano* **2019**, *13* (8), 8491–8494. https://doi.org/10.1021/acsnano.9b06394.

(21) Alhabeb, M.; Maleski, K.; Anasori, B.; Lelyukh, P.; Clark, L.; Sin, S.; Gogotsi, Y. Guidelines for Synthesis and Processing of Two-Dimensional Titanium Carbide ($Ti_3C_2T_x$ MXene). *Chem. Mater.* **2017**, *29* (18), 7633–7644. https://doi.org/10.1021/acs.chemmater.7b02847.

(22) Naguib, M.; Gogotsi, Y. Synthesis of Two-Dimensional Materials by Selective Extraction. *Acc. Chem. Res.* **2015**, *48* (1), 128–135. https://doi.org/10.1021/AR500346B.

(23) Bajraktarova-Valjakova, E.; Korunoska-Stevkovska, V.; Georgieva, S.; Ivanovski, K.; Bajraktarova-Misevska, C.; Mijoska, A.; Grozdanov, A. Hydrofluoric Acid: Burns and Systemic Toxicity, Protective Measures, Immediate and Hospital Medical Treatment. *Open Access Maced. J. Med. Sci.* **2018**, *6* (11), 2257–2269. https://doi.org/10.3889/OAMJMS.2018.429.

(24) Greaves, M.; Barg, S.; Bissett, M. A. MXene-Based Anodes for Metal-Ion Batteries. *Batter. Supercaps* **2020**, *3* (3), 214–235. https://doi.org/10.1002/BATT.201900165.

(25) Seh, Z. W.; Fredrickson, K. D.; Anasori, B.; Kibsgaard, J.; Strickler, A. L.; Lukatskaya, M. R.; Gogotsi, Y.; Jaramillo, T. F.; Vojvodic, A. Two-Dimensional Molybdenum Carbide (MXene) as an Efficient Electrocatalyst for Hydrogen Evolution. *ACS Energy Lett.* **2016**, *1* (3), 589–594. https://doi.org/10.1021/acsenergylett.6b00247.

(26) Yuan, W.; Cheng, L.; An, Y.; Wu, H.; Yao, N.; Fan, X.; Guo, X. MXene Nanofibers as Highly Active Catalysts for Hydrogen Evolution Reaction. *ACS Sustainable Chemistry and Engineering*. 2018, pp 8976–8982. https://doi.org/10.1021/acssuschemeng.8b01348.

(27) Liu, H.; Duan, C.; Yang, C.; Shen, W.; Wang, F.; Zhu, Z. A Novel Nitrite Biosensor Based on the Direct Electrochemistry of Hemoglobin Immobilized on MXene-Ti_3C_2. *Sensors Actuators B Chem.* **2015**, *218*, 60–66. https://doi.org/10.1016/J.SNB.2015.04.090.

(28) Holm, J. D.; Caplins, B. W. Introduction to STEM-in-SEM Part 1: Imaging and Diffraction with Common Commercially Available Transmission Detectors. *STEM SEM* **2020**, 1–20. https://doi.org/10.31399/ASM.TB.STEMSEM.T56000001.

(29) Holm, J. D.; Caplins, B. W. Introduction to STEM-in-SEM Part 2: Imaging and Diffraction with a Programmable Pixelated Detector. *STEM SEM* **2020**, 1–20. https://doi.org/10.31399/ASM.TB.STEMSEM.T56000001.

(30) Souvignier, B.; Wondratschek, H.; Aroyo, M. I.; Chapuis, G.; Glazer, A. M. Space Groups and Their Descriptions, In *International Tables for Crystallography, Volume A: Space Group Symmetry*, Aroyo, M. I.;

Wiley: West Sussex, 2016; pp 42–73 https://doi.org/10.1107/97809553602060000114.

(31) Dahlqvist, M.; Rosen, J. Predictive Theoretical Screening of Phase Stability for Chemical Order and Disorder in Quaternary 312 and 413 MAX Phases. *Nanoscale* **2020**, *12* (2), 785–794. https://doi.org/10.1039/c9nr08675g.

(32) Anasori, B.; Xie, Y.; Beidaghi, M.; Lu, J.; Hosler, B. C.; Hultman, L.; Kent, P. R. C.; Gogotsi, Y.; Barsoum, M. W. Two-Dimensional, Ordered, Double Transition Metals Carbides (MXenes). *ACS Nano* **2015**, *9* (10), 9507–9516. https://doi.org/10.1021/ACSNANO.5B03591.

(33) Burr, P. A.; Horlait, D.; Lee, W. E. Experimental and DFT Investigation of $(Cr,Ti)_3AlC_2$ MAX Phases Stability. *Mater. Res. Lett.* **2017**, *5* (3), 144–157. https://doi.org/10.1080/21663831.2016.1222598.

(34) Wang, C.; Shou, H.; Chen, S.; Wei, S.; Lin, Y.; Zhang, P.; Liu, Z.; Zhu, K.; Guo, X.; Wu, X.; Ajayan, P. M.; Song, L. HCl-Based Hydrothermal Etching Strategy toward Fluoride-Free MXenes. *Adv. Mater.* **2021**, *33* (27). https://doi.org/10.1002/ADMA.202101015.

(35) Juelsholt, M.; Anker, A. S.; Christiansen, T. L.; Jørgensen, M. R. V.; Kantor, I.; Sørensen, D. R.; Jensen, K. M. Ø. Size-Induced Amorphous Structure in Tungsten Oxide Nanoparticles. *Nanoscale* **2021**, *13* (47), 20144–20156. https://doi.org/10.1039/D1NR05991B.

(36) Anasori, B.; Shi, C.; Moon, E. J.; Xie, Y.; Voigt, C. A.; Kent, P. R. C.; May, S. J.; Billinge, S. J. L.; Barsoum, M. W.; Gogotsi, Y. Control of Electronic Properties of 2D Carbides (MXenes) by Manipulating Their Transition Metal Layers. *Nanoscale Horizons* **2016**, *1* (3), 227–234. https://doi.org/10.1039/C5NH00125K.

(37) Brox, B.; Olefjord, I. ESCA Studies of MoO_2 and MoO_3. *Surf. Interface Anal.* **1988**, *13* (1), 3–6. https://doi.org/10.1002/SIA.740130103.

(38) Olefjord, I.; Mathieu, H. J.; Marcus, P. Intercomparison of Surface Analysis of Thin Aluminium Oxide Films. *Surf. Interface Anal.* **1990**, *15* (11), 681–692. https://doi.org/10.1002/SIA.740151108.

(39) Kubitza, N.; Reitz, A.; Zieschang, A. M.; Pazniak, H.; Albert, B.; Kalha, C.; Schlueter, C.; Regoutz, A.; Wiedwald, U.; Birkel, C. S. From MAX Phase Carbides to Nitrides: Synthesis of V_2GaC, V_2GaN, and the Carbonitride $V_2GaC_{1-X}N_X$. *Inorg. Chem.* **2022**, *61* (28), 10634–10641. https://doi.org/10.1021/ACS.INORGCHEM.2C00200.

(40) Nansé, G.; Papirer, E.; Fioux, P.; Moguet, F.; Tressaud, A. Fluorination of Carbon Blacks: An X-Ray Photoelectron Spectroscopy Study: I. A Literature Review of XPS Studies of Fluorinated Carbons. XPS Investigation of Some Reference Compounds. *Carbon N. Y.* **1997**, *35* (2), 175–194. https://doi.org/10.1016/S0008-6223(96)00095-4.

(41) Ebner, J. R.; McFadden, D. L.; Walton, R. A. The X-Ray Photoelectron Spectra of Inorganic Molecules. XI1. Fluorine 1s Binding Energies in Metal Fluorides. *J. Solid State Chem.* **1976**, *17* (4), 447–449. https://doi.org/10.1016/S0022-4596(76)80016-3.

(42) Liu, J.; Peng, W.; Li, Y.; Zhang, F.; Fan, X. 2D MXene-Based Materials for Electrocatalysis. *Trans. Tianjin Univ.* **2020**, *26* (3), 149–171. https://doi.org/10.1007/s12209-020-00235-x.

(43) Balat, M.; Balat, H. Biogas as a Renewable Energy Sourcea Review. *Energy Sources, Part A Recover. Util. Environ. Eff.* **2009**, *31* (14), 1280–1293. https://doi.org/10.1080/15567030802089565.

(44) Turner, J. A. Sustainable Hydrogen Production. *Science* **2004**, *305* (5686), 972–974. https://doi.org/10.1126/SCIENCE.1103197/ASSET/B8AE2290-312A-4CBA-94B4-9968E7C7B725/ASSETS/GRAPHIC/ZSE0320427680001.JPEG.

(45) Tran, M. H.; Schäfer, T.; Shahraei, A.; Dürrschnabel, M.; Molina-Luna, L.; Kramm, U. I.; Birkel, C. S. Adding a New Member to the MXene Family: Synthesis, Structure, and Electrocatalytic Activity for the Hydrogen

Evolution Reaction of $V_4C_3T_x$. *ACS Appl. Energy Mater.* **2018**, *1* (8), 3908–3914. https://doi.org/10.1021/ACSAEM.8B00652.

(46) Zhu, J.; Cai, L.; Yin, X.; Wang, Z.; Zhang, L.; Ma, H.; Ke, Y.; Du, Y.; Xi, S.; Wee, A. T. S.; Chai, Y.; Zhang, W. Enhanced Electrocatalytic Hydrogen Evolution Activity in Single-Atom Pt-Decorated VS_2 Nanosheets. *ACS Nano* **2020**, *14* (5), 5600–5608. https://doi.org/10.1021/ACSNANO.9B10048/SUPPL_FILE/NN9B10048_SI_001.PDF.

(47) Wang, J.; Toby, B. H.; Lee, P. L.; Ribaud, L.; Antao, S. M.; Kurtz, C.; Ramanathan, M.; Von Dreele, R. B.; Beno, M. A. A Dedicated Powder Diffraction Beamline at the Advanced Photon Source: Commissioning and Early Operational Results. *Rev. Sci. Instrum.* **2008**, *79* (8), 879. https://doi.org/10.1063/1.2969260.

(48) Lee, P. L.; Shu, D.; Ramanathan, M.; Preissner, C.; Wang, J.; Beno, M. A.; Von Dreele, R. B.; Ribaud, L.; Kurtz, C.; Antao, S. M.; Jiao, X.; Toby, B. H. A Twelve-Analyzer Detector System for High-Resolution Powder Diffraction. *J. Synchrotron Radiat.* **2008**, *15* (5), 427–432. https://doi.org/10.1107/S0909049508018438/IE5021SUP1.PDF.

(49) Preissner, C.; Shu, D.; Toby, B. H.; Lee, P.; Wang, J.; Kline, D.; Goetze, K. The Sample-Changing Robot for the 11-BM High-Throughput Powder Diffraction Beamline. *Nucl. Instruments Methods Phys. Res. A* **2009**, *In press*.

(50) Dalesio, L. R.; Hill, J. O.; Kraimer, M.; Lewis, S.; Murray, D.; Hunt, S.; Watson, W.; Clausen, M.; Dalesio, J. The Experimental Physics and Industrial Control System Architecture: Past, Present, and Future. *Nucl. Inst. Methods Phys. Res. A* **1994**, *352* (1–2), 179–184. https://doi.org/10.1016/0168-9002(94)91493-1.

(51) Toby, B. H.; Von Dreele, R. B. GSAS-II: The Genesis of a Modern Open-Source All Purpose Crystallography Software Package. *J. Appl. Crystallogr.* **2013**, *46* (2), 544–549. https://doi.org/10.1107/S0021889813003531/HTTPS://JOURNALS-IUCR-ORG.EZPROXY1.LIB.ASU.EDU/SERVICES/RSS.HTML.

(52) Chupas, P. J.; Qiu, X.; Hanson, J. C.; Lee, P. L.; Grey, C. P.; Billinge, S. J. L. Rapid Acquisition Pair Distribution Function (RA-PDF) Analysis. *J. Appl. Crystallogr.* **2003**. *36,* 1342–1347. https://doi.org/10.1107/S0021889803017564

(53) Prescher, C.; Prakapenka, V. B. DIOPTAS: A Program for Reduction of Two-Dimensional X-Ray Diffraction Data and Data Exploration. *High Pressure Res.* **2015**, *35* (3), 223–230. https://doi.org/10.1080/08957959.2015.1059835.

(54) Juhás, P.; Davis, T.; Farrow, C. L.; Billinge, S. J. L. PDFgetX3: A Rapid and Highly Automatable Program for Processing Powder Diffraction Data into Total Scattering Pair Distribution Functions. *J. Appl. Crystallogr.* **2013**, *46* (2), 560–566. https://doi.org/10.1107/S0021889813005190.

(55) Yang, X.; Juhas, P.; Farrow, C. L.; Billinge, S. J. L.; Yang, X.; Juhas, P.; Farrow, C. L.; Billinge, S. J. L. XPDFsuite: An End-to-End Software Solution for High Throughput Pair Distribution Function Transformation, Visualization and Analysis. 2014, *arXiv.* https://doi.org/10.48550/arXiv.1402.3163 (accessed January 13, 2023)

(56) Farrow, C. L.; Juhas, P.; Liu, J. W.; Bryndin, D.; Boin, E. S.; Bloch, J.; Proffen, T.; Billinge, S. J. L. PDFfit2 and PDFgui: Computer Programs for Studying Nanostructure in Crystals. *J. Phys. Condens. Matter* **2007**, *19* (33). https://doi.org/10.1088/0953-8984/19/33/335219.

(57) Rueden, C. T.; Schindelin, J.; Hiner, M. C.; DeZonia, B. E.; Walter, A. E.; Arena, E. T.; Eliceiri, K. W. ImageJ2: ImageJ for the next Generation of Scientific Image Data. *BMC Bioinformatics* **2017**, *18* (1). https://doi.org/10.1186/S12859-017-1934-Z.

(58) Caplins, B. W.; Holm, J. D.; White, R. M.; Keller, R. R. Orientation Mapping of Graphene Using 4D STEM-in-

SEM. *Ultramicroscopy* **2020**, *219*, 113137. https://doi.org/10.1016/J.ULTRAMIC.2020.113137.

(59) Lee, T. L.; Duncan, D. A. A Two-Color Beamline for Electron Spectroscopies at Diamond Light Source. *Synchrotron Radiat. News* **2018**, *31* (4), 16–22. https://doi.org/10.1080/08940886.2018.1483653.

(60) Shinotsuka, H.; Tanuma, S.; Powell, C. J.; Penn, D. R. Calculations of Electron Inelastic Mean Free Paths. X. Data for 41 Elemental Solids over the 50eV to 200keV Range with the Relativistic Full Penn Algorithm. *Surf. Interface Anal.* **2015**, *47* (9), 871–888. https://doi.org/10.1002/SIA.5789.

For Table of Contents Only

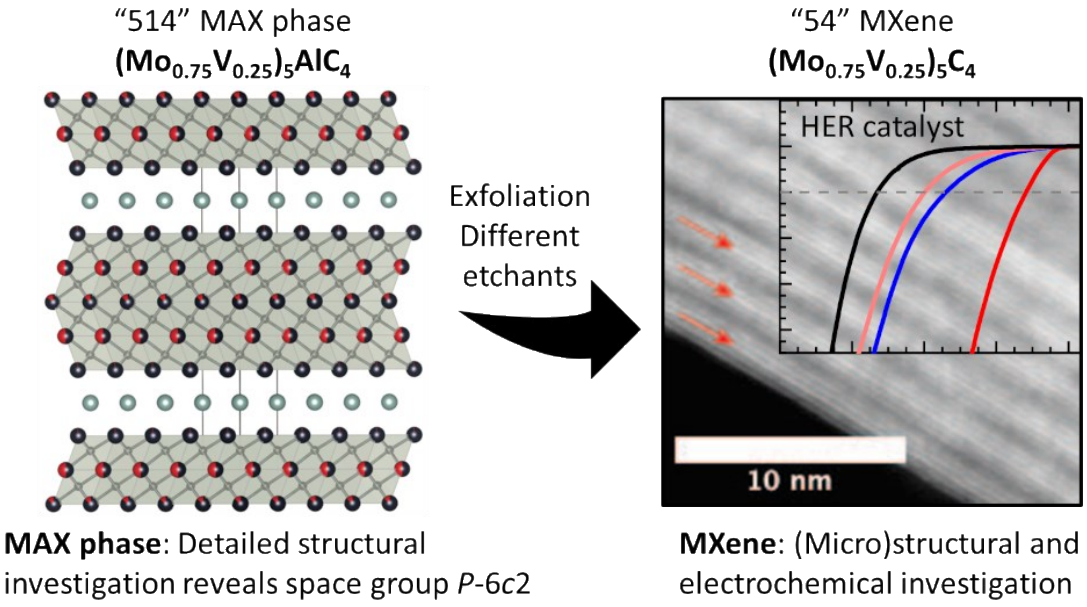

MAX phase: Detailed structural investigation reveals space group *P*-6*c*2

MXene: (Micro)structural and electrochemical investigation